

Deep Supervised LSTM for 3D morphology estimation from Multi-View RGB Images of Wheat Spikes

Olivia Zumsteg^{a,*}, Nico Graf^b, Aaron Häusler^{c,1}, Norbert Kirchgessner^a, Nicola Storni^a, Lukas Roth^a and Andreas Hund^a

^aETH Zurich, Institute of Agricultural Science, Universitätsstrasse 2, Zurich, 8092, Switzerland

^bETH Zurich, Department of Computer Science, Universitätsstrasse 6, Zurich, 8902, Switzerland

^cETH Zurich, Department of Mechanical and Process Engineering, Leonhardstrasse 21, Zurich, 8092, Switzerland

ARTICLE INFO

Keywords:

2D-to-3D prediction

Volume phenotyping

Deep supervision

Multi-view learning

ABSTRACT

Estimating three-dimensional morphological traits from two-dimensional RGB images presents inherent challenges due to the loss of depth information, projection distortions, and occlusions under field conditions. In this work, we explore multiple approaches for non-destructive volume estimation of wheat spikes, using RGB image sequences and structured-light 3D scans as ground truth references. Due to the complex geometry of the spikes, we propose a neural network approach for volume estimation in 2D images, employing a transfer learning pipeline that combines DINOv2, a self-supervised Vision Transformer, with a unidirectional Long Short-Term Memory (LSTM) network. By using deep supervision, the model is able to learn more robust intermediate representations, which enhances its generalisation ability across varying evaluation sequences. We benchmark our model against two conventional baselines: a 2D area-based projection and a geometric reconstruction using axis-aligned cross-sections. Our deep supervised model achieves a mean absolute percentage error (MAPE) of 6.46% on six-view indoor images, outperforming the area (9.36%) and geometric (13.98%) baselines. Fine-tuning the model on field-based single-image data enables domain adaptation, yielding a MAPE of 10.82%. We demonstrate that object shape significantly impacts volume prediction accuracy, with irregular geometries such as wheat spikes posing greater challenges for geometric methods compared to our deep learning approach.

1. Introduction

Accurate volume estimation plays a critical role across a range of industrial and agricultural applications. In logistics and warehousing, volume measurement informs optimization tasks such as truck loading and material flow management (Artaso and López-Nicolás, 2016), while in manufacturing, it contributes to quality assurance and defect prevention (Wasayangkool et al., 2022). In the context of food production and processing, volume serves as a non-destructive proxy for various biological traits, enabling tasks such as fruit growth monitoring, plant phenotyping, post-harvest handling, size-based sorting, and quality grading of horticultural products (Mon and ZarAung, 2020; Su et al., 2017; Koc, 2007) in a non-destructive way (Moreda et al., 2009).

Within crop research, wheat spikes represent a particularly relevant plant organ for structure and volumetric analysis. The wheat inflorescence (spike or head) produces short side branches, called spikelets, along a central main axis (rachis). The spikelets are arranged in an alternating pattern

and terminate with a single spikelet at the end of the rachis (Gao et al., 2019). This renders the wheat spike symmetric with a dorsiventral view in which most of the bracts and bract-like structures enclosing the florets are visible and a lateral view in which the rachis and some bracts are visible (Lersten, 1987). Recent literature refers to the dorsiventral and lateral views as frontal and side views, respectively (Niu et al., 2024). Thus, the overall volume of this structure is complex given the shape of the different branches carrying the florets. Due to this irregular shapes, we hypothesize that a geometrical feature extraction to predict volume might not be sufficient for accurate volume prediction.

Fruiting efficiency is the final result of the fate of floret development and is defined as the number of grains set per unit of spike dry weight at flowering. Fruiting efficiency reflects the overall efficiency of a genotype with which resources are used to set grains (Slafer et al., 2015), and was proposed as a promising trait to improve yield-potential (Pretini et al., 2021). We hypothesize that the spike dry weight at flowering correlates with the spike volume at flowering, and can therefore be approximated by the spike volume. We propose to term the total volume of spikes in a canopy at flowering, i.e., the summed volume per area of

*Corresponding author

 olivia.zumsteg@usys.ethz.ch (O. Zumsteg)

ORCID(s):

all individual spikes as "fruiting capacity". Environmental stresses encountered during spike development, such as low radiation, often reduce spike volume and, by extension, the fruiting capacity (Anderegg et al., 2024). Scalable, image-based prediction of spike volume might facilitate the identification of high-performing genotypes with improved resilience to climate-induced stressors up to heading, enabling to dissect yield into its components.

Understanding the relationship between spike phenotypes and wheat yield is essential for selecting wheat genotypes, as these traits show significant positive correlations with wheat yield. However, efficient spike phenotyping methods are limited, particularly in-field where light conditions are complex, and only few studies have successfully segmented individual spikes from field-collected LiDAR (Light Detection and Ranging) data (Liu et al., 2023). The authors showed that spike length estimates were highly accurate with their LiDAR measurements ($R^2 = 0.99$). However, spike volume constructed from the point cluster of the spike was not evaluated with manual measurements. Wang et al. (2022) used structured light scanners on a field mobile platform to generate 3D point clouds of wheat plants in the field. The authors estimated wheat spike volume using small cuboids fitted to the shape of the spikes. However, accurately capturing the detailed structure of the spikes requires a large number of cuboids, which increases computational cost and processing time (Zhang et al., 2025).

Based on the existing literature, we conclude that estimating the volume of wheat spikes is challenging due to their irregular and complex geometry. Here, we propose a novel method that circumvents the limitations of previous approaches with a 2D image-based deep learning approach:

- We present a practical and accurate method for predicting wheat spike volume directly from 2D RGB images. We assess the influence of object shape on the performance of two baseline methods, as well as our unidirectional deeply supervised DINOv2-LSTM model.
- We systematically investigate the impact of varying number of views on prediction accuracy, assessing the robustness of each approach under conditions of limited visual information.
- We investigate the generalisability of the proposed deep learning model by evaluating its performance in

field conditions, both with and without fine-tuning on field data.

- We constructed a comprehensive, high-quality dataset comprising over 1,700 wheat spikes from more than 90 genotypes across multiple developmental stages, each captured from several viewpoints. This dataset is complemented by 3D ground truth obtained through structured-light scanning.

The subsequent sections of this paper are organised as follows: Section 2 reviews related work on conventional 2D and 3D volume estimation methods, and advances in deep learning for phenotyping. Section 3 provides an in-depth description of our proposed spike volume estimation approach. Section 4 details the comparative analysis of the algorithms and models. Section 5 discusses the accuracy of various volume prediction methods, as well as the impact of image count on evaluation accuracy. Section 6 concludes the paper with a summary of the key findings.

2. Related Work

One common approach to measuring volume is to make use of depth information from stereo vision or active sensors like structured light devices. Stereo vision reconstructs depth from multiple view points using feature matching and camera parameters (Seitz et al., 2006). Structured light systems compute depth by projecting patterns and applying triangulation, based on the angle and baseline between projector and camera (Rachakonda et al., 2019). Given the high cost and complexity associated with stereo structured light systems, numerous studies have explored 2D and 3D image-based techniques for volume estimation.

2.1. Volume Estimation via 2D Geometric Features

In 2D computer vision systems, volume is commonly estimated by extracting geometric features (Moreda et al., 2009). The volume is approximated by the area, length, or shapes like cylinders, spheres, or ellipsoids. Such approaches have been applied to various agricultural products, including tomatoes (Uluişik et al., 2018), oranges (Khostehnazhand et al.), lemons (Vivek Venkatesh et al., 2015), and different citrus fruits on multiple images (Omid et al., 2010), or on apples (Iqbal et al., 2011), and eggs (Soltani et al., 2015) on single images. While such approaches are effective for regularly shaped objects, they might perform

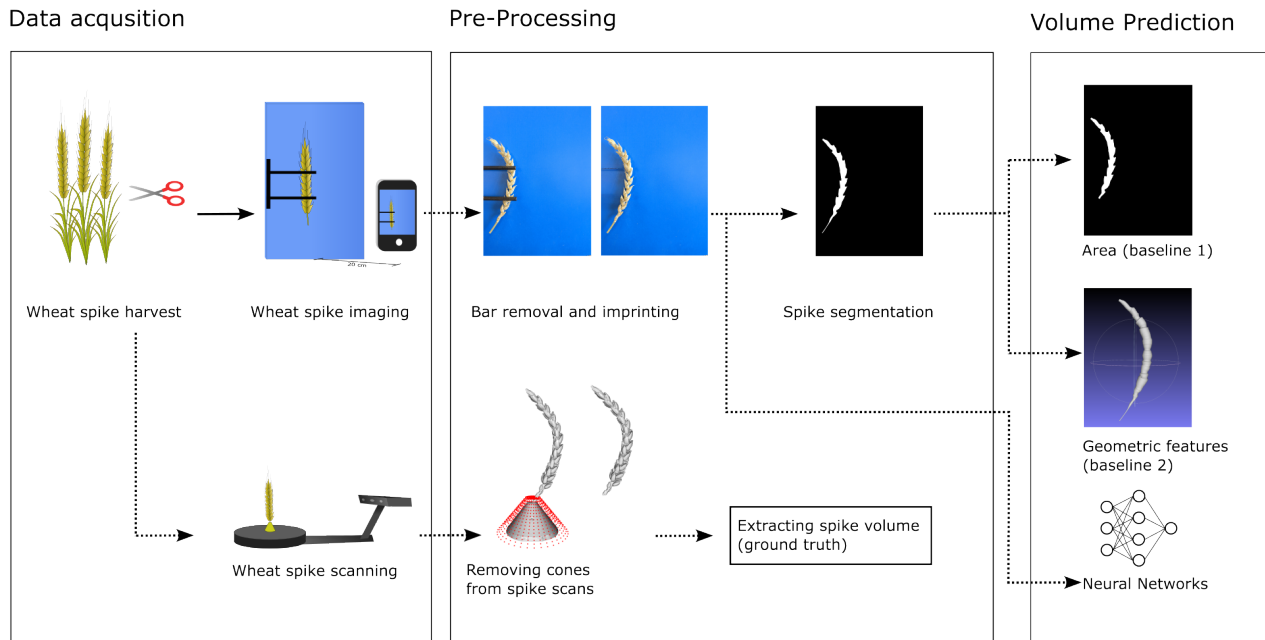


Figure 1: Overview of the study design separated in three sections data acquisition, pre-processing, and volume prediction. In the data acquisition step, wheat spikes were sampled, imaged, and scanned. Images were pre-processed to get the binary segmentations masks. The scans were processed and the ground truth volume was extracted. Two baselines, and neural networks were used to estimate wheat spike volume based on images.

poorly on irregular or highly non-uniform shapes, where simple geometric approximations introduce significant error.

2.2. Depth-based Volume Estimation

3D computer vision methods overcome some of these issues by reconstructing depth from multiple views or by generating point clouds. This often requires camera parameters or fixed poses (Cho et al., 2018; Liu et al., 2011). Numerous 3D reconstruction-based applications were used in food volume estimation. Applications include food volume estimation using idealized geometric shapes (Xu et al., 2013), stereo reconstruction (Dehais et al., 2017), or depth maps from single RGB images (Graikos et al., 2020). Alternatively, depth data can be captured with Time-of-Flight (ToF) cameras, which emit IR (Infra-Red) light to determine depth values for each pixel from which the 3D structure of the scene can be estimated (Hansard et al., 2013). The depth value is provided by projecting an IR light wave which is then reflected from the object and captured by the camera's IR sensor. However, depth cameras do not perform well under strong illumination, such as natural outdoor light conditions. The IR components in natural light tend to confuse the IR sensors of the depth cameras (Haider and Hel-Or, 2022) making these depth cameras unsuitable

for measuring spike volume directly in field. In contrast to ToF technologies, LiDAR uses laser pulses to create plant point clouds. These sensors provide point clouds of plant interception points, allowing to measure 3D traits such as tree volume (Rosell Polo et al., 2009) and above-ground biomass of wheat (Jimenez-Berni et al., 2018). However, wind-induced movements of the plants can increase noise and reduce the accuracy of the 3D reconstruction (Dassot et al., 2011).

2.3. Advances in Deep Learning for Phenotyping

Machine learning offers an alternative when input-output relationships are non-linear or complex (O' Mahony et al., 2017). In recent years, deep learning has been widely adopted for computer vision tasks such as image colourisation, object detection, semantic segmentation, and classification. With the availability of GPUs, machine learning libraries and large training datasets, these networks have improved the performance of such tasks since their revival in 2012 by Krizhevsky et al. (2017) and O'Mahony et al. (2020). Hybrid methods combine segmentation and depth prediction to estimate volume from RGB and depth images (Lo et al., 2018). Others rely on single-view RGB input, using feature extraction and depth reconstruction to build

point clouds and estimate volume (Dalai et al., 2023). Recent approaches eliminate the need for calibration by using neural networks to predict depth from RGB images alone (Kim et al., 2025). However, the dependence on depth sensors can limit the applicability of this approach. Furthermore, Steinbrener et al. (2023) used Mask R-CNN and LSTM networks to estimate volume from monocular video without camera reference or setup constraints.

3. Methods

In the following, we first describe the procedure of acquiring images of the wheat spikes and collecting the corresponding measured volumes. Subsequently, two traditional baseline models are presented to predict the spike volume from images. The first model is based on the pixel area, while the second utilises geometrical features of the spikes. Finally, we introduce our proposed neural network, which predicts the spike volume directly from images.

3.1. Data Acquisition and Processing

The experiment was carried out in the field phenotyping platform (FIP, (Kirchgessner et al., 2016)) at the ETH plant research station Lindau-Eschikon, Switzerland (47.449°N, 8.682°E, 520 m.a.s). Wheat spikes were collected from the trait calibration panel planted in the FIP. This panel consisted of i) historic varieties from Switzerland, France and Germany covering important post-green revolution varieties, ii) varieties included in variety registration in Switzerland, and iii) a diverse set of variety widely tested in the framework of the EU projects INVITE and PHENET.

3.1.1. Wheat Spike Sampling

Wheat spikes are complex-shaped objects that occur in various forms. To create a diverse dataset, spikes of 83 and 82 different genotypes were sampled in 2023 and 2024, respectively, with 72 overlapping genotypes. Furthermore, 120 spikes consisting of two different genotypes from a shading experiment in 2023 were included. Shading tents, mounted before flowering, reduced spike volume up to -36.5 % (Anderegg et al., 2024), and therefore increased dataset diversity. Sampling occurred three times in each season: (i) at flowering (June 9, 2023, June 10, 2024 and June, 2024); (ii) between flowering and maturity (June 29, 2023, July 4, 2023 and July 5, 2024); and (iii) at maturity (July 11, 2023 and July 19, 2024). Furthermore, 100 spikes were randomly

sampled at flowering in 2024 to calculate the correlation between spike dry weight and volume at flowering.

3.1.2. Wheat Spike Imaging

For image acquisition, we built a custom imaging setup consisting of a camera rig (Universal Mobile Phone Cage, SmallRig Technology (HK) Limited, New York, USA) a smartphone with a 12.2 megapixel camera (Google Pixel 6a, Google LLC, USA) and a blue screen (Kömatex blue 891, Röhm AG, Brüttsellen, Schweiz) with an 3D-printed object holder consisting of two black 3D-printed plastic bars (Figure 2, a). The camera rig was fixed at 20 cm from the background using aluminum poles resulting in a ground sampling distance of 0.05 mm/px.

We created two main imaging datasets. The indoor dataset consists of spikes that were imaged from six different angles to gather a wide range of viewing geometries. The spikes were imaged from both sides, i.e. two images were taken from both the frontal and side view, respectively. Two additional images were taken in an oblique position between the two views (Figure 2, b). This resulted in a total of six images taken in the three different viewing geometries. Note that because of the twisted shape of some spikes, it was often not possible to capture all their spikelets in exactly the same view. However, across the six images taken per spike, all three viewing geometries were generally represented.

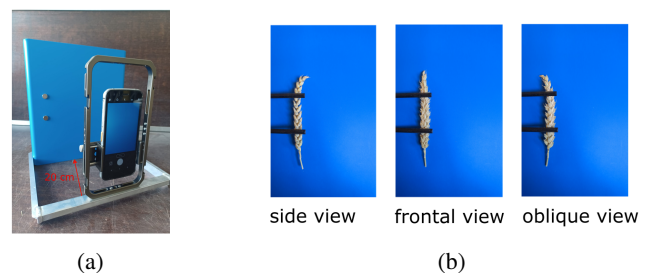


Figure 2: Overview of the camera setup and image acquisition process. The imaging setup with a 20 cm distance between the camera and a blue background panel (a). Representative images of a frontal, side, and oblique view of the wheat spike (b).

The second imaging dataset was collected in-field in 2023, where 843 spikes were additionally imaged directly in-field prior to sampling. Due to the presence of awns, each spike was imaged only from the side perspective. The operator pointed the imaging setup in a way to avoid direct sunlight on either the object or lens of the phone to minimise direct shadows and lens flare, respectively.

3.1.3. Wheat Spike Scanning

After imaging, objects were scanned using a structured-light 3D scanner (Shining 3D Einscan-SE V2, SHINING3D, Hangzhou, China) to approximate the volume and use it as ground truth volume. The number of turnable steps of the turning table were set to 12. This setting allowed for a fast scanning of the objects while maintaining high volume accuracy. The high dynamic range (HDR) was used to help with high contrasting objects. Each object was fixed in a plastic cone to avoid movements during the scanning process. After scanning an object, the scanner software (EXScan S Version 3.1.4.3 (Windows)) was used to convert the obtained 3D point cloud into a triangular mesh surface in a watertight fashion, which fills all holes directly, and with the highest accuracy possible. The meshes were then exported as Polygon File Format (ply).

3.1.4. Pre-Processing of Images and Scans

The pre-processing phase focused on processing the images and object meshes to generate datasets for establishing baselines and training neural networks. During these process steps, black bars were removed from the images, and the wheat spikes were segmented to obtain the baseline dataset. To approximate the ground truth volume, the cone was removed and the remaining volume was extracted.

3.1.5. Image Bar Removal and Inpainting

In a first step, the plastic bars that held the spike in place during imaging were removed. This step aimed to enable generalised volume predictions independent of the specific imaging setup, and to compute the area and geometric baselines. The removal process consisted of two main steps: (i) segmenting the bars; and (ii) inpainting the segmented regions to preserve the visual integrity of the wheat spike (Figure 3, a and b). Segmentation was performed using Segment Anything, a robust and adaptable segmentation algorithm proposed by Kirillov et al. (2023), which performs well under varying lighting conditions. We used the official Python API, running the pre-trained Segment Anything Model (SAM) locally. The model weights, available at <https://github.com/facebookresearch/segment-anything>, were downloaded and used for inference. For each image, we identified a point on the bar by selecting the darkest pixels within a region where the bar was expected to appear. We determined the darkest pixels by analysing the brightness profile of the leftmost 5% of the image in the

HSV Value channel. Local minima in the vertical brightness profile, indicating dark regions were extracted using peak detection on the inverted signal. The corresponding y-coordinates of these minima were paired with a fixed x-coordinate of half the width of the analysed strip. The binary bar masks generated by SAM, along with the corresponding RGB images, were then passed to the inpainting algorithm developed by Yu et al. (2019), which reconstructs the occluded image regions in a visually coherent manner. The inpainting model is accessible at https://github.com/JiahuiYu/generative_inpainting.

3.1.6. Spike Segmentation

To compute the area and geometrical baselines, full-spike segmentations were performed following the removal of the fixation bars, utilizing again SAM (Kirillov et al., 2023). As in the bar segmentation process, the initial step required identification of the target object (i.e. the spike) within the RGB image. To identify a seed point on the spike, we converted the image to HSV colour space and applied a color-based mask to isolate regions with hue values corresponding to orange tones ($\text{hue} \in [10, 25]$). This mask was further refined by retaining only pixels with high saturation and brightness values. The coordinates of the identified seed point was supplied for object segmentation. The resulting binary masks delineating the spike regions were used for the area and geometric baseline calculation (Figure 3, c).

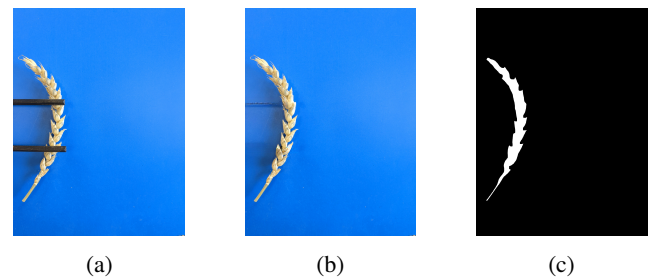


Figure 3: Overview of preprocessing steps, including an original image (a), after bar removal and inpainting (b), and after segmentation (c).

3.1.7. Volume extraction as ground truth

The reconstructed object meshes obtained from the scanning process included both the wheat spike and the supporting cone used for stabilization during scanning. To isolate the spike volume, it was necessary to first remove the underlying cone, as illustrated in Figure 4, a and b. Cone removal was facilitated by the consistent placement of the

cones across all scans, wherein the vertical position (z -coordinate) remained fixed, and only the horizontal (x and y) coordinates required determination. This localization was achieved by identifying the minimum and maximum extent of the cone along the x - and y -axes and computing the midpoint to approximate the cone's central axis. Combined with a predefined apex height and a known base radius at the cone's z -level, these parameters enabled the reconstruction of a cone-shaped volume, which was subsequently removed from the mesh to isolate the spike geometry. Subsequent volume computation was performed using the Python libraries PyMeshLab (Muntoni et al., 2023) and Open3D (Zhou et al., 2018), which provide efficient tools for processing and analysing 3D mesh data.



Figure 4: 3D meshes before (a) and after cone removal (b).

3.2. Volume Prediction

To evaluate the hypothesis that neural networks can enhance volume prediction for complex-shaped objects, we compared their performance to two baseline models of varying complexity. The dataset of wheat spikes was split based on genotypes into training, validation, and test sets in a 70%, 10%, and 20% ratio. The dataset was split based on genotypes to prevent overfitting and ensure that the model does not learn genotype-specific features. The first, simpler area-baseline was computed by counting the number of pixels belonging to the spike, and analysing their correlation with the ground truth volume. The second, more advanced geometrical baseline incorporates manually extracted shape features, such as height and radius, to model volume using a non-linear function. While the area baseline assumes a direct linear relationship between surface area and volume, the geometrical baseline accounts for more complex spatial dependencies. All models, including the neural networks, were evaluated on the same test set to ensure a consistent performance comparison. As evaluation metrics, we used Pearson's correlation coefficient, the coefficient of determination (R^2), and the mean absolute percentage error (MAPE).

3.3. Area Baseline

For the area baseline, spike area was quantified by computing the number of foreground pixels in the binary segmentation masks, where each pixel with a value of one represented part of the spike and zero indicated background. The average pixel count for the six masks was interpreted as a proxy for the 2D projected area of the spike. This baseline served to assess the extent to which simple 2D information could approximate volumetric measurements.

3.4. Geometrical Baseline

The geometrical baseline is based on the assumption that the spike's volume increases non-linearly with its radius and that its cross-section can be approximated as circular along its longitudinal axis. To estimate the volume, the spike was treated as a series of stacked discs with varying radii. The procedure consisted of the following steps: (i) binary spike mask generation via segmentation using the Segment Anything Model (SAM), as described in subsection 3.1.6; (ii) extraction of the spike's skeleton to approximate its central axis; (iii) fitting a parameterized smoothing spline along this axis to represent its curvature; (iv) computing the spike's width orthogonal to the spline at multiple sampled points along its length; and (v) estimating the total volume by integrating the cross-sectional area ($\pi * r^2$) along the length of the spline. This approach captured geometric variability and allowed for a more realistic volumetric approximation than purely 2D metrics.

The skeleton of the spike within the binary segmentation mask was computed using the thinning algorithm proposed by Zhang and Suen (1984) as illustrated in Figure 5a.

To extract the main axis of the spike (Figure 5b), we applied a custom recursive algorithm (Algorithm 1) that operates on the skeleton. Starting from an initial point, the algorithm traverses the skeleton by recursively exploring all neighbouring pixels and identifying the longest continuous path, which is then returned as the spike's main axis.

In Algorithm 1, $N(p)$ denotes the set of 8-connected neighbors of point p within S . Specifically, for a point $p = (i, k)$, we define $N(p) = \{\tilde{p} \in S : \tilde{p} \in (i \pm 1, k \pm 1)\}$.

We then defined the smoothed central axis of the spike as

$$g(t) = (f_x(t), f_y(t)),$$

Algorithm 1 Find_Main_Axis

Input: skeleton pixel mask S , starting point p
 $path \leftarrow [p]$
 Remove p from S
 Remove $N(p)$ from S
 $subpaths \leftarrow []$
for $\tilde{p} \in N(p)$ **do**
 $tmp \leftarrow \text{Find_Main_Axis}(S, \tilde{p})$
 Append tmp to $subpaths$
end for
 $maxpath \leftarrow \arg \max_{z \in subpaths} \text{length}(z)$
 $path \leftarrow \text{concatenate}(path, maxpath)$
return $path$

where $f_x(t)$ and $f_y(t)$ are cubic B-spline functions fitted to the x - and y -coordinates of the axis points over the normalized parameter $t \in [0, 1]$.

To compute the physical length of the spike, the function g is re-scaled using a constant pixel-to-millimeter ratio (assumed consistent across the dataset due to standardized image acquisition), and integrated as follows:

$$L = \int_0^1 \left\| \frac{d}{dt} g(t) \right\| dt.$$

The main advantage of spline fitting is its continuous differentiability, which allows for robust computation of orthogonal vectors along the curve. This enables us to measure the width of the spike orthogonal to the axis g at multiple positions.

From these measurements, we derive a radius function $r : [0, 1] \rightarrow \mathbb{R}_+$, which gives the spike radius along its length. Assuming circular cross-sections, the total volume is estimated by:

$$V = \pi \int_0^L \left(r \left(\frac{t}{L} \right) \right)^2 dt.$$

We approximate this integral using the trapezoidal rule with 600 evenly spaced evaluation points. Higher-order quadrature methods were avoided due to spline smoothness limitations. The resulting volume is visualized in Figure 5c.

3.4.1. Peduncle Removal

To improve the volume prediction accuracy of the area baseline model, we refined the binary segmentation mask by removing the peduncle present at the bottom of the spike (Figure 6). The peduncle length varied between spikes and

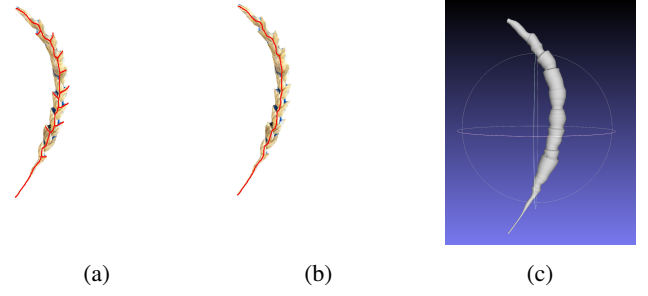


Figure 5: Visualization of the geometrical baseline, including the skeleton of a spike (a), defined main axis (b), and the final spike volume approximation (c)

did not contribute meaningfully to the target volume, thereby introducing unwanted variability. Using the previously computed main axis (obtained via a spline fitted to the skeletonized mask), orthogonal cross-sections were computed to estimate the spike's width at 200 equidistant points along its length. Starting from the bottom, the algorithm searched for the first instance where the width increased by more than 4% relative to the previous section. This point was heuristically identified as the transition from peduncle to spike. Based on the position and orientation at this transition, a rectangular mask region was constructed using tangent and normal vectors derived from the spline geometry (Figure 6a). All pixels within the box were converted to background (Figure 6b). This geometric refinement ensured consistent spike-only masks across samples.

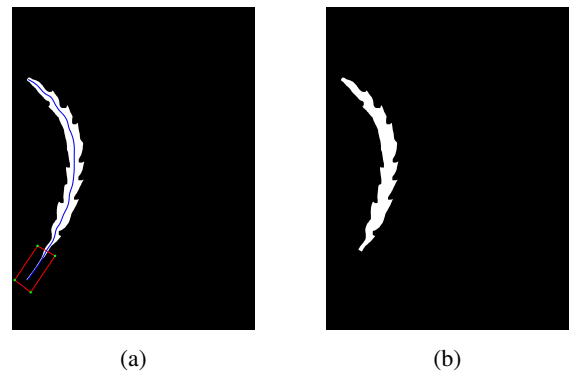


Figure 6: Binary mask with identified peduncle (red box, a), and after peduncle removal (b).

3.5. Neural Network

Images can be processed by neural networks which then directly predict volumes. Our workflow is illustrated in Figure 7. All input images were downsampled from their original resolution of 3024 x 4032 pixels to 256 x 341 pixels using bilinear interpolation with anti-aliasing enabled, and subsequently center-cropped to 244 x 244 pixels to align with the input size required by downstream pre-trained networks. Re-sizing prior to cropping ensured that the object remains visible post-cropping. The additional cropping step served to remove peripheral image regions (e.g., blue borders) and emphasized the central object. To augment the dataset and improve model generalisation, images were randomly flipped horizontally and vertically with a probability of 0.5. The measured spike volume was normalized using the empirical mean and standard deviation of the training set to facilitate stable optimization.

To take advantage of models pre-trained on large datasets, we employed DINOv2, a self-supervised Vision Transformer model, to extract intermediate image embeddings suitable for general visual understanding tasks (Oquab et al., 2024). Pre-trained model weights were obtained from the official repository <https://github.com/facebookresearch/dinov2>, and the small variant was selected, producing embeddings of dimension 384. Pixel intensities of input images were normalized using the channel-wise mean and standard deviation of the ImageNet dataset to ensure compatibility with the input distribution anticipated by Dinov2. Subsequently, each image was passed through the DINOv2 encoder. The sequence of embeddings, representing different views of the sample plant, were then fed into a Long Short-Term Memory network (LSTM). LSTMs are a type of recurrent neural network (RNN) with the ability to learn and predict sequential data of varying length by capturing information from previous time steps.

The LSTM architecture consisted of an input size of 384, three hidden layers of size 512, CeLU activations, and dropout regularization ($p = 0.5$).

3.5.1. Training Procedure

Due to the imbalance in the volume distribution, where more samples are clustered around the mean, we used a scaled MSE loss similar to Ren et al. (2022). In this loss, the sample is scaled inversely proportional to its frequency in the dataset:

$$\mathcal{L}_{\text{Scaled}} = \frac{1}{N} \sum_{i=1}^N w_i (y_i - \hat{y}_i)^2. \quad (1)$$

where N denotes the number of samples, y_i is the measured volume for the i -th sample, \hat{y}_i is the corresponding predicted volume, and w_i is a weighting factor used to scale the squared error of the i -th sample.

The weights w_i were calculated using an inverse frequency approach based on histogram binning of denormalized volume values. Samples in under-represented bins (extremely small or large volumes) received higher weights,

$$w_i = \frac{1}{\max\{w'_k : 1 \leq k \leq N\}} w'_i, \quad w'_i = \frac{1}{\text{freq}(b_i)}, \quad (2)$$

where b_i denotes the bin index of sample i . The weights are then normalized to have a maximum value of 1.

We implemented two different approaches for generating the output from the LSTM. In the sequence-to-one setup, only the final hidden state was used and passed through a linear layer to predict a single scalar volume per spike (Figure 8a). In the sequence-to-sequence setup, the linear layer was applied to each LSTM output, resulting in one scalar prediction per input image (Figure 8b). This corresponds to a deep supervision approach, where supervision is also applied to hidden layers (Li et al., 2022).

Therefore, the input to the scaled loss was adapted to

$$\mathcal{L}_{\text{Scaled}} = \frac{1}{N} \sum_{i=1}^N \sum_{j=1}^6 w_i (y_i - \hat{y}_{ij})^2, \quad (3)$$

where j denotes the six images per spike.

The model was trained on all six images for 5000 epochs with a batch size of 32, using the Adam optimizer. The learning rate started at 1×10^{-4} decreasing linearly to 1×10^{-6} over the course of training. The model corresponding to the lowest validation loss was selected as the final model. This model was then evaluated using six, four, two and one image(s), corresponding to random angles. The same model was evaluated on the field images with one side view per spike. Additionally, the same model was fine-tuned using field images of spikes from the training set. During fine-tuning, the learning rate decreased linearly from 1×10^{-5} to 1×10^{-6} , batch size was set to 16, and the volume was

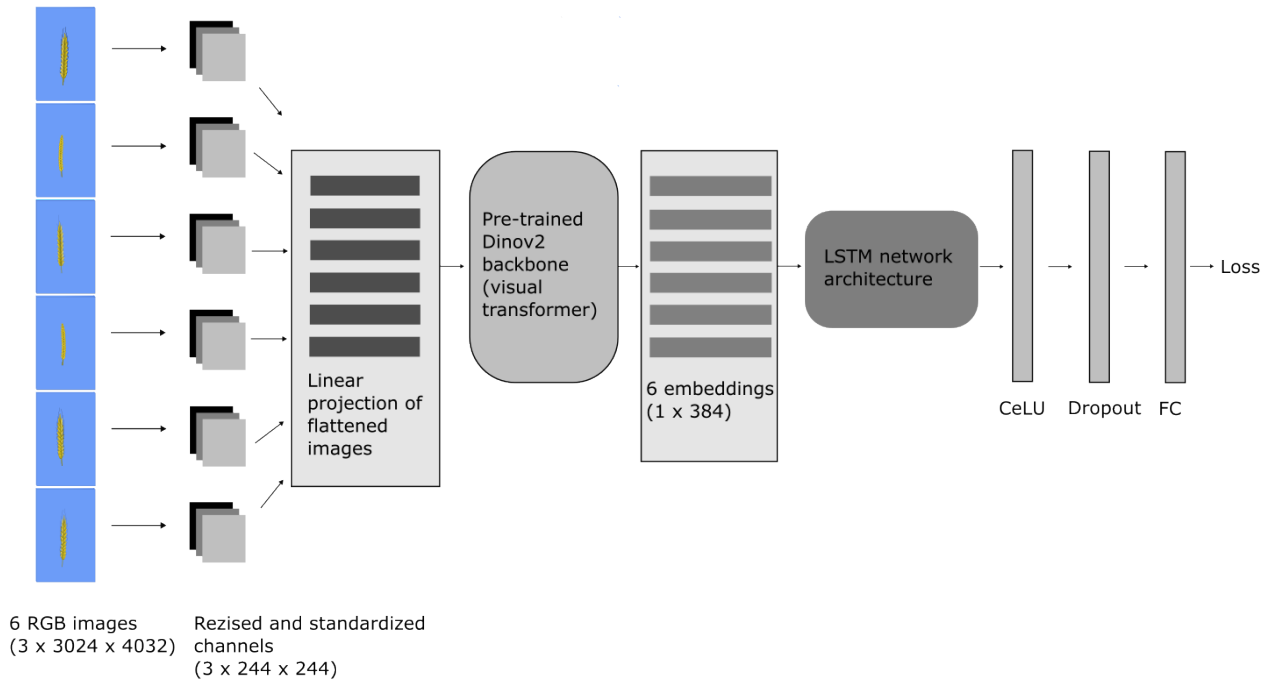
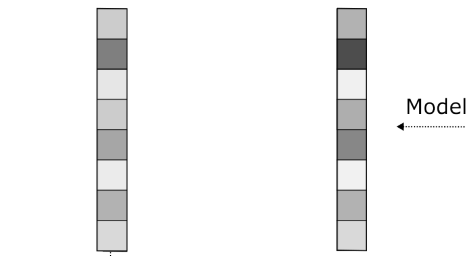


Figure 7: Overview of the neural network workflow trained on six images. After image re-sizing and normalizing, DINOv2 was used to extract embeddings from linear projections of the six images (dark grey, horizontal boxes). The embeddings (light grey, horizontal boxes) were subsequently passed through the LSTM layers, followed by a CeLU activation, a dropout layer, a fully connected layer, and finally the loss function.

Sequence-to-One Setup:

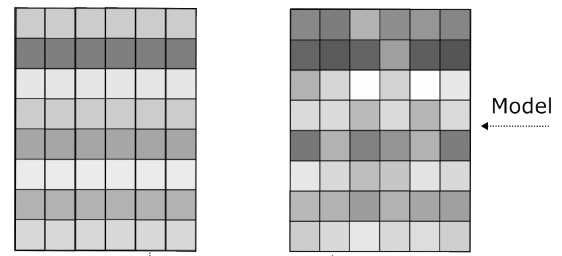
True volume (batch size) Predicted volume (batch size)



$$\mathcal{L}_{\text{Scaled}} = \frac{1}{N} \sum_{i=1}^N w_i (y_i - \hat{y}_{ij})^2$$

Sequence-to-Sequence Setup:

True volume (batch size x 6 images) Predicted volume (batch size x 6 images)



$$\mathcal{L}_{\text{Scaled}} = \frac{1}{N} \sum_{i=1}^N \sum_{j=1}^6 w_i (y_i - \hat{y}_{ij})^2$$

Figure 8: Sequence-to-one setup (a), and sequence-to-sequence setup (b) used to train volume prediction on 6 input images per spike

normalized during training using the mean and standard deviation of the field image training set.

4. Results

We found a high correlation between spike dry weight and the measured spike volume at flowering of 100 spikes (Figure 9). Hence, our assumption that the spike volume might serve as a key yield-related trait, indicating an upper bound on grain-filling potential, is justified. Fruiting efficiency is defined as the number of grains set per unit of spike dry weight at flowering. Consequently, estimating total spike volume across a field at flowering can provide an approximation of the maximum attainable yield for a given genotype under ideal conditions.

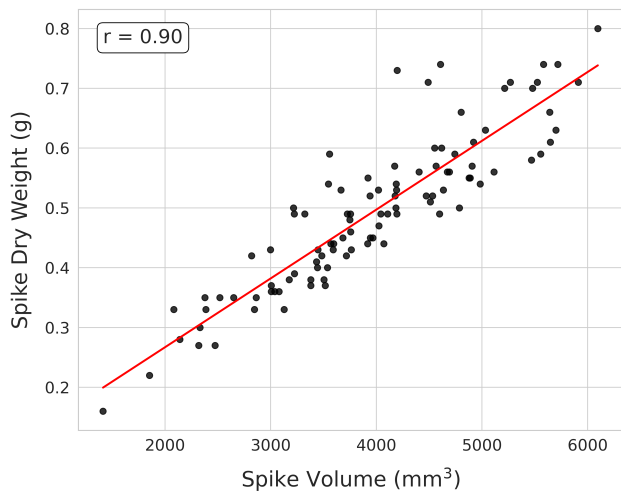


Figure 9: Scatter plot with linear regression between spike volume measured by structured-light 3D scanning and dry weight at flowering measured. Measurements were taken in 2024. Each point represents one spike.

Figure 10 shows the volume distribution of the small shaded panel sampled in 2023 (a), the regular panel sampled in 2023 (b), and the regular panel sampled in 2024 (c), as well as the number of sampled spikes. Mean volume of the earliest sampling group was smaller, compared to second and the third sampling. Furthermore, the means of the small panel, containing shaded spike, are lower compared to the regular panels, increasing the diversity in wheat spikes in the dataset (Table 1).

We evaluated our LSTM-based deep learning model against two conventional baselines, the 2D area-based method and a geometric model assuming cylindrical cross-sections (Table 2). Correlation, coefficient of determination (R^2), and mean absolute percentage error (MAPE) were used

as performance metrics across different numbers of input images (six, four, two, and one). Among the baselines, the geometric baseline consistently performed worse across all image counts. A deep supervision approach (sequence-to-sequence) was necessary to enable evaluation on fewer images than used during trained. With this, the LSTM model achieved a higher correlation and R^2 , and lower MAPE than both baseline methods. With six images, the LSTM reached a correlation of 0.94 and a MAPE of 6.46%, compared to a correlation of 0.87% and a MAPE of 9.363% for the best-performing baseline (area-based).

As expected, prediction error declined as the number of evaluation images increased. However, even with an evaluation on only one of the six images per spike, the LSTM model achieved a correlation of 0.89 and a MAPE of 9.48%. This is similar to the area baseline method evaluated on all six images.

To better understand how prediction accuracy varies across developmental stages and growing seasons, we visualized the correlation between the predicted and measured volumes for the six and one image evaluation case (Figure 11). No discernible pattern or clustering tendency was visible among the sampling groups, indicating the absence of clear outlier groups or group-specific trends. Minor deviations could be observed in some late season samples, likely reflecting increased morphological variability or a smaller number of genotypes exhibiting particularly large volumes in the training dataset.

Figure 12 presents the decrease in MAPE as a function of the number of evaluation images, comparing the two baseline methods with the LSTM model. While all methods showed improvements with more evaluation images, the performance gains of the baseline methods began to level-off beyond two images. Specifically, the MAPE of the area baseline decreased by 13.60% from one to two images, 6.03% from two to four images, and 2.30% from four to six images. The geometric baseline follows a similar pattern, with reductions of 17.67%, 6.93%, and 1.46%, respectively. In contrast, the LSTM model showed a stronger benefit from additional images, with MAPE decreasing by 20.76% from one to two images, 10.73% from two to four images, and 3.65% from four to six images, showing a steady reduction in prediction error as the number of input images increases.

Wheat Spike Volume Estimation

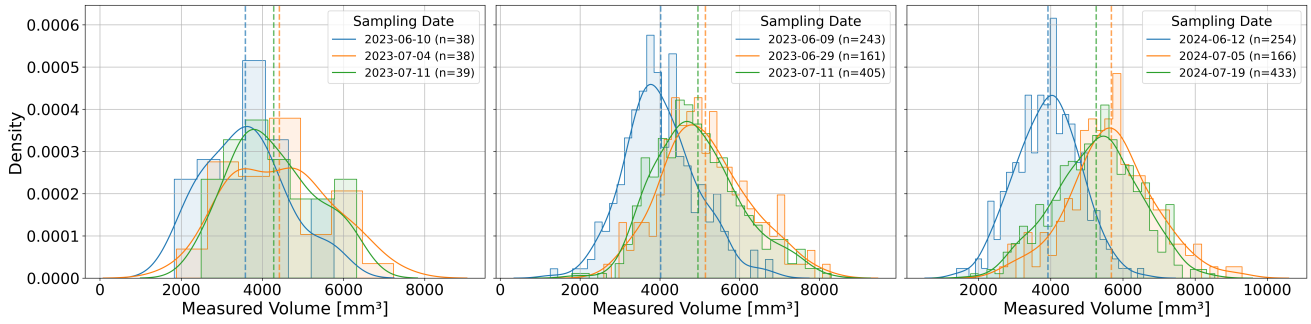


Figure 10: Measured spike volume distribution of the smaller shaded panel in 2023 (a), the regular panel in 2023 (b), and the regular panel in 2024 (c), as well as the number of sampled spikes. The mean of the distribution is represented as a dashed line.

Table 1

Mean volume (in mm^3) for each sampling date across groups.

Sampling Date	2023 shaded	2023	2024
2023-06-10 / 2023-06-09 / 2024-06-12	3583.24	4019.84	3921.87
2023-07-04 / 2023-06-29 / 2024-07-05	4421.58	5143.01	5678.33
2023-07-11 / 2023-07-11 / 2024-07-19	4280.17	4956.93	5258.91

4.1. Field-Image Prediction

As additional task, we assessed the neural network’s capability to generalise to field images. Fine-tuning on a subset of field-based images was essential to facilitate the domain transfer. Compared to the model trained on indoor images only, the MAPE decreased from 21.72% to 10.82% (Table 3). Fine-tuning on field images also reduced volume over-estimation of 645.47 mm^3 to 124.49 mm^3 , suggesting

that the fine-tuned model learned to account for features such as awns and variable lighting (Figure 13).

4.2. Runtime Performances

We evaluated both the training time (in seconds per epoch) and the evaluation time (in seconds per spike) of the manual volume measurement and the proposed neural network (Table 4). All models were executed on an NVIDIA RTX 5000 GPU. Manual volume measurements with the

Table 2

Correlation, R^2 , and MAPE of measured and predicted spikes volumes for different image counts. The LSTMs were trained on six images in the sequence-to-one, or sequence-to-sequence setup. Models were evaluated on six, four, two, and one image(s), respectively.

Algorithm	Six images			Four images		
	Correlation	R^2	MAPE	Correlation	R^2	MAPE
<i>Baselines</i>						
Area baseline	0.87	0.74	9.36	0.87	0.74	9.58
Geometric baseline	0.81	0.28	13.98	0.81	0.31	14.18
<i>Neural Networks</i>						
LSTM (sequence-to-one)	0.94	0.88	6.51	0.94	0.87	6.96
LSTM (sequence-to-sequence)	0.94	0.88	6.46	0.94	0.88	6.71
Algorithm	Two images			One image		
	Correlation	R^2	MAPE	Correlation	R^2	MAPE
<i>Baselines</i>						
Area baseline	0.84	0.69	10.20	0.81	0.62	11.80
Geometric baseline	0.78	0.15	15.24	0.69	-0.15	18.51
<i>Neural Network</i>						
LSTM (sequence-to-one)	0.91	0.59	13.78	0.82	0.03	21.503
LSTM (sequence-to-sequence)	0.93	0.85	7.51	0.89	0.79	9.48

Wheat Spike Volume Estimation

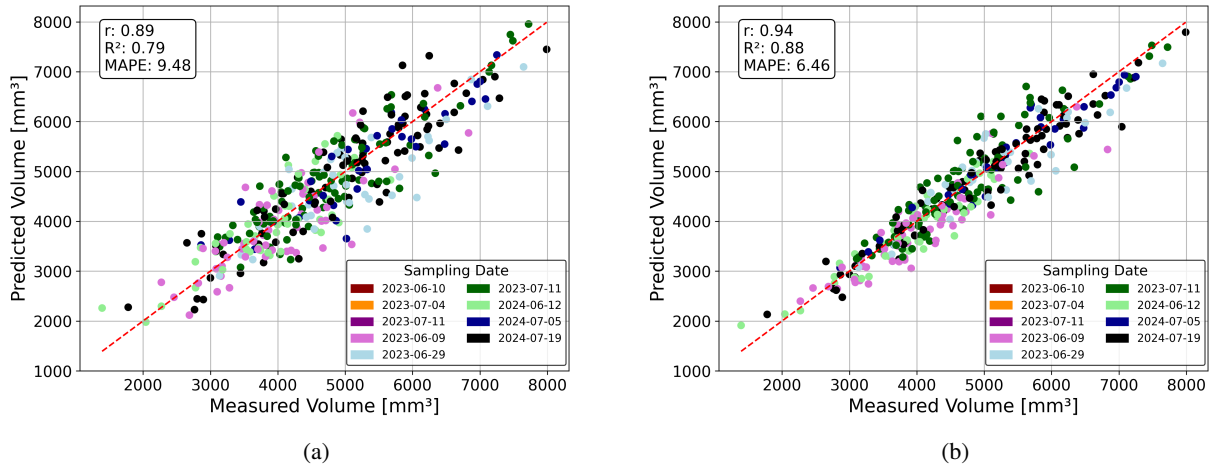


Figure 11: Correlation, R^2 , and MAPE of measured and predicted volumes of the LSTM trained on six images and evaluated on one (a) and on six images (b). Each point represents a single spike of the test set, with color coding indicating the sampling date across the two years. The red line represents a perfect correlation.

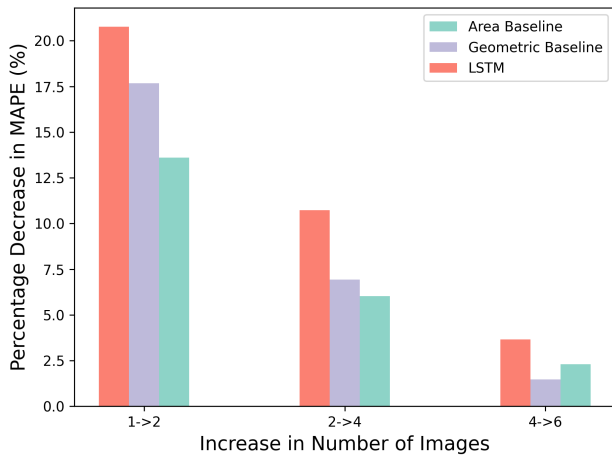


Figure 12: Decrease of Mean Absolute Percentage Error of baselines and the neural network based on different numbers of images.

Table 3

Correlation, R^2 , and MAPE for baselines and LSTM models trained with varying input settings, evaluated on one field image.

Model Configuration	Correlation	R^2	MAPE
LSTM	0.71	-0.03	21.72
LSTM (fine-tuned)	0.84	0.69	10.82

3D scanner take around 300 seconds per spike. Training the LSTM takes up to 2.5 seconds per epoch with a batch size of 32, but achieved an efficient inference with an evaluation time of 0.002 seconds per spike and per image.

Table 4

Comparison of manual measurement and model performance in terms of approximated time for training and evaluation.

Method	Training Time (s/epoch)	Evaluation Time (s/spike)
Structured light scanner	-	300
LSTM (per image)	2.5	0.002

5. Discussion

The goal of this study was to develop a practical and scalable method to estimate the volume of the wheat spike. Manual volume estimation methods including structured light scanning, is time-consuming and labor-intensive. More advanced 3D vision systems, including 3D reconstruction, require specialized hardware and precise intrinsic and extrinsic camera calibration to reliably infer depth. This reliance on controlled environments and expensive equipment makes such methods impractical for high-throughput phenotyping. Although neural networks are increasingly applied to volume estimation tasks, only few approaches target wheat spike volume. However, accurate spike phenotyping is necessary due to its correlation with yield. Current methods remain limited, particularly under challenging field conditions.

While some studies focus on grain volume estimation (Walker and Panozzo, 2012, 2011; Alamery and Salman Al-Badri, 2023), their approach requires threshing prior to volume measurement. Lately, there has been a growing interest in CT-based methods to estimate grain volume

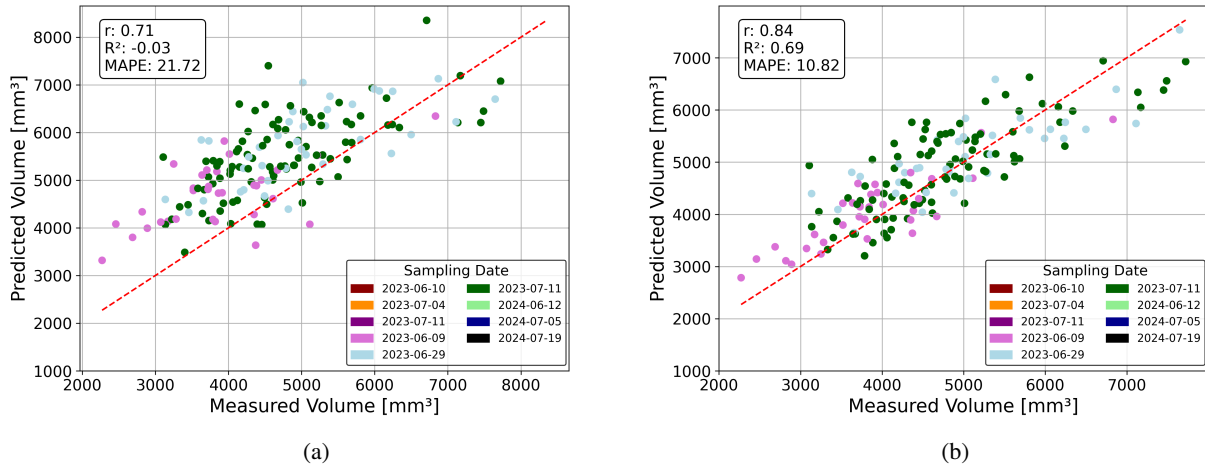


Figure 13: Correlation, R^2 , and MAPE of measured and predicted volumes of the LSTM trained on six indoor images, and evaluated on one field image (a). Fine-tuned LSTM model using field images and evaluated on one image (b). Each point represents a single spike of the test set, with color coding indicating the sampling date across the two years. The red line represents a perfect correlation

(Strange et al., 2015; Hughes et al., 2017; Xiong et al., 2019; Zhou et al., 2021). However, such estimates typically lack a direct connection to externally visible traits such as the spike volume. Closing the gap between internal (grain) and external (spike) phenotyping could be a significant step forward in high-throughput yield estimation.

5.1. Improving single image predictions

While LSTMs have shown effective results in domains such as speech recognition or language translation, they have also shown good performances in image or video classification tasks (Islam et al., 2020; Chen et al., 2023; Al-jabery et al., 2020). In these approaches, similarly to ours, features were first extracted from images and then fed into an LSTM to model sequential dependencies across the image sequence. Code examples show that usually the final state of the LSTM is taken for classification or regression tasks (van der Weth, 2019), while in tasks such as sequence labelling, it is recommended to use all hidden outputs for prediction (Alexandru, 2017). We could show that training the model on sequences of six images while predicting the spike volume based on fewer images leads to high errors when relying solely on the final time step. By adapting the model's output to incorporate all time steps during training, the network learns to improve predictions at each step. Since the measured volume is the same for all the six images per plant, the model ability to predict the volume based on each

single image is increased, ultimately allowing it to make accurate predictions from a single image during evaluation, resulting in both improved performance and faster evaluation.

5.2. Comparison between baselines and neural network

Across all image counts, the LSTM model consistently outperforms both the area-based and geometric baselines in terms of correlation, R^2 , and MAPE. This performance gap reflects fundamental differences in how these methods handle the complex geometry of wheat spikes. The area baseline assumes a linear relationship between 2D projected area and 3D volume, which over-simplifies the structural variability of spikes, particularly features like curvature, which do not scale linearly with area. The geometric baseline improves upon this by modelling the spike as a series of discs with circular cross-sections, but this still relies on strong geometric assumptions (e.g., axial symmetry and smooth radius profiles). These assumptions can break down in real-world cases, such as spikes with irregular contours, or non-uniform curvature. In contrast, the LSTM-based neural network makes no prior assumptions about the object's geometry. Instead, it might learn complex spatial representations directly from raw pixel data, and using color information across multiple views. The use of DINOv2 embeddings enables the model to extract features from each image, while the LSTM captures cross-view dependencies,

allowing it to synthesize a more complete understanding of the 3D volume. These learned representation proves more effective at modelling morphological variations, leading to significantly lower prediction errors. While these results demonstrate the power of deep learning for spike volume estimation, they also raise an important question: to what extent does the shape of the object influence the accuracy of different estimation methods?

5.3. Effect of object shape on model performance

Object shape plays a critical role in the success of volume estimation methods. Our results align with prior research on irregularly shaped objects, such as tomatoes (Uluişik et al., 2018), and contrasts with results on more geometrically regular objects like oranges (Khojastehnazhand et al.), where estimation accuracy tends to be higher. The relatively higher error observed for tomatoe volume has been attributed to their irregular shapes resulting in concavity and increasing the prediction error (Uluişik et al., 2018). A similar issue arises with wheat spikes. While they may appear roughly axis-symmetric from a side view, the spikelets are positioned in an alternating way along the main axis. Furthermore, the spikelets slightly vary in shape and size. This results in an asymmetrical radius on either side of the main axis, making volume prediction using the geometric baseline more challenging. Integrating information on the viewing angle and adapting volume calculation to imaging perspective, as demonstrated in apple volume estimation with shape-specific models (Iqbal et al., 2011), may improve accuracy in such cases.

Our area baseline, which estimates the spike volume using the average pixel area across multiple views, presumably mitigates errors by balancing volume over- and underestimation from different views. Interestingly, for objects with highly regular, axis-symmetric shapes, such as eggs, 2D area-based methods have even out-performed by neural networks in terms of R^2 score (Soltani et al., 2015). These results further underscore the importance of object shape on the success of different volume estimation approaches.

5.4. Effect of image count in evaluation

While all methods benefit from increasing the number of evaluation images, the magnitude of improvement differs substantially between the baselines and the LSTM model. This suggests that the neural network is capable of integrating complementary geometric cues from multiple

view points to build a more complete internal representation of object volume. Moreover, these results highlight a key strength of deep learning: the ability to learn flexible, non-linear mappings from raw image features to volumetric predictions. However, the improved performance with additional views also underscores the importance of large and diverse training datasets. The model's ability to generalise across a broad range of spike geometries depends on being exposed to sufficient variability during training. Evaluating our LSTM model on random views enables predictions that are independent of the viewing angle. However, in indoor settings, using multiple images per spike is recommended, as it results in higher prediction accuracy. In contrast, for field conditions, the model was evaluated using a single side view, which was chosen because it facilitates image capturing of spikes with awns.

5.5. Generalisability to field images

Although the neural network achieves a low prediction error evaluated on a single indoor image, the same model does not generalise well to single field images. Fine-tuning the model using field images from the training dataset reduced the volume over-estimation. This over-estimation is likely due to the presence of awns and varying lighting conditions in the field setting. One approach for improvement could be to investigate whether the Global Wheat Full Semantic Organ Segmentation (GWFS) benchmark model (Wang et al., 2025) trained to treat awns as invisible, could be used to pre-segment spikes. This pre-processing step may enable less biased volume estimation.

6. Conclusion

Fruiting efficiency is a promising trait for improving wheat yield but traditionally requires destructive harvests. Our results show that spike volume closely correlates with spike dry weight at anthesis, allowing for non-destructive estimation of this trait. By employing a vision-based LSTM architecture on multiple RGB image views, we achieve improvements in volumetric prediction over our baselines that rely on area projection or geometric approximations. Our results reveal that object shape plays a critical role in prediction performance, with irregular and asymmetric geometries, such as those of wheat spikes, posing challenges to assumption-driven models. In contrast, our deep supervised model benefits from learned intermediate representations

that generalize well across varying input views. Furthermore, we show that domain adaptation through fine-tuning on single-view field images enables the model to retain predictive accuracy in field environments. Future directions might include incorporating organ segmentation models to improve in-field predictions, and scale-up wheat volume prediction by means of 3D proximal sensing.

7. Data availability

The full dataset, the source code and the trained models will be made publicly available through the ETH research collection after publication.

CRedit authorship contribution statement

Olivia Zumsteg: Writing – review & editing, Writing – original draft, Visualisation, Validation, Software, Methodology.. **Nico Graf:** Writing – review & editing, Visualisation, Software, Methodology.. **Aaron Häusler:** Writing – review & editing, Visualisation, Software, Methodology.. **Norbert Kirchgessner:** Writing – review & editing, Software, Methodology.. **Nicola Storni:** Writing – review & editing, Software, Methodology.. **Lukas Roth:** Writing – review & editing, Methodology, Supervision.. **Andreas Hund:** Writing – review & editing, Methodology, Supervision, Conceptualisation, Funding acquisition.

8. CRedit authorship contribution statement

The authors declare that they have no known competing financial interests or personal relationships that could have appeared to influence the work reported in this paper.

9. Acknowledgement

We thank Konstantina Gkouramani, Mohammad Hosein Fakhrosae, and Patrick Fitzi, for their invaluable support with data collection. We are grateful to Prof. Achim Walter for providing funding for this work. Special thanks to Nico Graf and Aaron Häuser for their contributions to data analysis, and to Nicola Storni and Dr. Norbert Kirchgessner for their technical support. We also appreciate the supervision provided by PD Dr. Andreas Hund and Dr. Lukas Roth throughout the project.

References

- Al-jabery, K.K., Obafemi-Ajayi, T., Olbricht, G.R., Wunsch II, D.C., 2020. 4 - Selected approaches to supervised learning, in: Al-jabery, K.K., Obafemi-Ajayi, T., Olbricht, G.R., Wunsch II, D.C. (Eds.), *Computational Learning Approaches to Data Analytics in Biomedical Applications*. Academic Press, pp. 101–123. doi:10.1016/B978-0-12-814482-4.00004-8.
- Alamery, M.S., Salman Al-Badri, S.B., 2023. Determination the Wheat Weight and Volume: Mathematical Approach. *IOP Conference Series: Earth and Environmental Science* 1213, 012103. doi:10.1088/1755-1315/1213/1/012103.
- Alexandru, A., 2017. Sequence models tutorial. URL: https://github.com/pytorch/tutorials/blob/main/beginner_source/nlp/sequence_models_tutorial.py. accessed on 2025-06-19.
- Anderegg, J., Kirchgessner, N., Aasen, H., Zumsteg, O., Keller, B., Zenkl, R., Walter, A., Hund, A., 2024. Thermal imaging can reveal variation in stay-green functionality of wheat canopies under temperate conditions. *Frontiers in Plant Science* 15. doi:10.3389/fpls.2024.1335037.
- Artaso, P., López-Nicolás, G., 2016. Volume estimation of merchandise using multiple range cameras. *Measurement* 89, 223–238. doi:10.1016/j.measurement.2016.04.005.
- Chen, J., Wang, J., Yuan, Q., Yang, Z., 2023. CNN-LSTM Model for Recognizing Video-Recorded Actions Performed in a Traditional Chinese Exercise. *IEEE Journal of Translational Engineering in Health and Medicine* 11, 351–359. doi:10.1109/JTEHM.2023.3282245.
- Cho, W., Shin, M., Jang, J., Paik, J., 2018. Robust pedestrian height estimation using principal component analysis and its application to automatic camera calibration, in: 2018 International Conference on Electronics, Information, and Communication (ICEIC), pp. 1–2. doi:10.23919/ELINFOCOM.2018.8330602.
- Dalai, R., Dalai, N., Senapati, K.K., 2023. An accurate volume estimation on single view object images by deep learning based depth map analysis and 3D reconstruction. *Multimedia Tools and Applications* 82, 28235–28258. doi:10.1007/s11042-023-14615-7.
- Dassot, M., Constant, T., Fournier, M., 2011. The use of terrestrial LiDAR technology in forest science: Application fields, benefits and challenges. *Annals of Forest Science* 68, 959–974. doi:10.1007/s13595-011-0102-2.
- Dehais, J., Anthimopoulos, M., Shevchik, S., Mougiakakou, S., 2017. Two-View 3D Reconstruction for Food Volume Estimation. *IEEE Transactions on Multimedia* 19, 1090–1099. doi:10.1109/TMM.2016.2642792.
- Gao, X.Q., Wang, N., Wang, X.L., Zhang, X.S., 2019. Architecture of Wheat Inflorescence: Insights from Rice. *Trends in Plant Science* 24, 802–809. doi:10.1016/j.tplants.2019.06.002.
- Graikos, A., Charisis, V., Iakovakis, D., Hadjidimitriou, S., Hadjileontiadis, L., 2020. Single Image-Based Food Volume Estimation Using Monocular Depth-Prediction Networks. *Universal Access in Human-Computer Interaction. Applications and Practice* 12189, 532–543. doi:10.1007/978-3-030-49108-6_38.
- Haider, A., Hel-Or, H., 2022. What Can We Learn from Depth Camera Sensor Noise? *Sensors* 22, 5448. doi:10.3390/s22145448.
- Hansard, M., Lee, S., Choi, O., Horaud, R., 2013. *Time-of-Flight Cameras: Principles, Methods and Applications*. SpringerBriefs in Computer Science, Springer, London. doi:10.1007/978-1-4471-4658-2.
- Hughes, A., Askew, K., Scotson, C.P., Williams, K., Sauze, C., Corke, F., Doonan, J.H., Nibau, C., 2017. Non-destructive, high-content analysis of wheat grain traits using X-ray micro computed tomography. *Plant Methods* 13, 76. doi:10.1186/s13007-017-0229-8.

- Iqbal, S.Md., Gopal, A., Sarma, A.S.V., 2011. Volume estimation of apple fruits using image processing, in: 2011 International Conference on Image Information Processing, pp. 1–6. doi:10.1109/ICIIP.2011.6108909.
- Islam, M.Z., Islam, M.M., Asraf, A., 2020. A combined deep CNN-LSTM network for the detection of novel coronavirus (COVID-19) using X-ray images. *Informatics in Medicine Unlocked* 20, 100412. doi:10.1016/j.imu.2020.100412.
- Jimenez-Berni, J.A., Deery, D.M., Rozas-Larraondo, P., Condon, A.T.G., Rebetzke, G.J., James, R.A., Bovill, W.D., Furbank, R.T., Sirault, X.R.R., 2018. High Throughput Determination of Plant Height, Ground Cover, and Above-Ground Biomass in Wheat with LiDAR. *Frontiers in Plant Science* 9. doi:10.3389/fpls.2018.00237.
- Khojastehnazhand, M., Omid, M., Tabatabaefar, A., . Determination of orange volume and surface area using image processing technique. *Int. Agrophys.* .
- Kim, J.h., Lee, D.s., Kwon, S.k., 2025. Volume Estimation Method for Irregular Object Using RGB-D Deep Learning. *Electronics* 14, 919. doi:10.3390/electronics14050919.
- Kirchessner, N., Liebisch, F., Yu, K., Pfeifer, J., Friedli, M., Hund, A., Walter, A., 2016. The ETH field phenotyping platform FIP: A cable-suspended multi-sensor system. *Functional plant biology: FPB* 44, 154–168. doi:10.1071/FP16165.
- Kirillov, A., Mintun, E., Ravi, N., Mao, H., Rolland, C., Gustafson, L., Xiao, T., Whitehead, S., Berg, A.C., Lo, W.Y., Dollár, P., Girshick, R., 2023. Segment Anything. doi:10.48550/arXiv.2304.02643, arXiv:2304.02643.
- Koc, A.B., 2007. Determination of watermelon volume using ellipsoid approximation and image processing. *Postharvest Biology and Technology* 45, 366–371. doi:10.1016/j.postharvbio.2007.03.010.
- Krizhevsky, A., Sutskever, I., Hinton, G.E., 2017. ImageNet classification with deep convolutional neural networks. *Communications of the ACM* 60, 84–90. doi:10.1145/3065386.
- Lersten, N.R., 1987. Morphology and Anatomy of the Wheat Plant, in: *Wheat and Wheat Improvement*. John Wiley & Sons, Ltd. chapter 2, pp. 33–75. doi:10.2134/agronmonogr13.2ed.c2.
- Li, R., Wang, X., Huang, G., Yang, W., Zhang, K., Gu, X., Tran, S.N., Garg, S., Alty, J., Bai, Q., 2022. A comprehensive review on deep supervision: Theories and applications. URL: <https://arxiv.org/abs/2207.02376>, arXiv:2207.02376.
- Liu, J., Collins, R., Liu, Y., 2011. Surveillance Camera Autocalibration Based on Pedestrian Height Distributions. doi:10.5244/C.25.117.
- Liu, Z., Jin, S., Liu, X., Yang, Q., Li, Q., Zang, J., Li, Z., Hu, T., Guo, Z., Wu, J., Jiang, D., Su, Y., 2023. Extraction of Wheat Spike Phenotypes From Field-Collected Lidar Data and Exploration of Their Relationships With Wheat Yield. *IEEE Transactions on Geoscience and Remote Sensing* 61, 1–13. doi:10.1109/TGRS.2023.3333344.
- Lo, F.P.W., Sun, Y., Qiu, J., Lo, B., 2018. Food Volume Estimation Based on Deep Learning View Synthesis from a Single Depth Map. *Nutrients* 10, 2005. doi:10.3390/nu10122005.
- Mon, T., ZarAung, N., 2020. Vision based volume estimation method for automatic mango grading system. *Biosystems Engineering* 198, 338–349. doi:10.1016/j.biosystemseng.2020.08.021.
- Moreda, G.P., Ortiz-Cañavate, J., García-Ramos, F.J., Ruiz-Altisent, M., 2009. Non-destructive technologies for fruit and vegetable size determination – A review. *Journal of Food Engineering* 92, 119–136. doi:10.1016/j.jfoodeng.2008.11.004.
- Muntoni, A., jmespadero, Cignoni, P., Luaces, A., RichardScottOZ, luzpaz, Zhang, F., 2023. Cnr-isti-vclab/PyMeshLab: PyMeshLab v2023.12. Zenodo. doi:10.5281/zenodo.10363967.
- Niu, Z., Liang, N., He, Y., Xu, C., Sun, S., Zhou, Z., Qiu, Z., 2024. A Novel Method for Wheat Spike Phenotyping Based on Instance Segmentation and Classification. *Applied Sciences* 14, 6031. doi:10.3390/app14146031.
- O’ Mahony, N., Murphy, T., Panduru, K., Riordan, D., Walsh, J., 2017. Real-time monitoring of powder blend composition using near infrared spectroscopy, pp. 1–6. doi:10.1109/ICSenST.2017.8304431.
- O’Mahony, N., Campbell, S., Carvalho, A., Harapanahalli, S., Hernandez, G.V., Krpalkova, L., Riordan, D., Walsh, J., 2020. Deep Learning vs. Traditional Computer Vision, in: Arai, K., Kapoor, S. (Eds.), *Advances in Computer Vision*. Springer International Publishing, Cham. volume 943, pp. 128–144. doi:10.1007/978-3-030-17795-9_10.
- Omid, M., Khojastehnazhand, M., Tabatabaefar, A., 2010. Estimating volume and mass of citrus fruits by image processing technique. *Journal of Food Engineering* 100, 315–321. doi:10.1016/j.jfoodeng.2010.04.015.
- Oquab, M., Darcet, T., Moutakanni, T., Vo, H., Szafraniec, M., Khalidov, V., Fernandez, P., Haziza, D., Massa, F., El-Nouby, A., Assran, M., Ballas, N., Galuba, W., Howes, R., Huang, P.Y., Li, S.W., Misra, I., Rabbat, M., Sharma, V., Synnaeve, G., Xu, H., Jegou, H., Mairal, J., Labatut, P., Joulin, A., Bojanowski, P., 2024. DINOv2: Learning Robust Visual Features without Supervision. doi:10.48550/arXiv.2304.07193, arXiv:2304.07193.
- Pretini, N., Alonso, M.P., Vanzetti, L.S., Pontaroli, A.C., González, F.G., 2021. The physiology and genetics behind fruiting efficiency: A promising spike trait to improve wheat yield potential. *Journal of Experimental Botany* 72, 3987–4004. doi:10.1093/jxb/erab080.
- Rachakonda, P.K., Muralikrishnan, B., Sawyer, D.S., 2019. Sources of Errors in Structured Light 3D Scanners. NIST .
- Ren, J., Zhang, M., Yu, C., Liu, Z., 2022. Balanced MSE for Imbalanced Visual Regression, in: 2022 IEEE/CVF Conference on Computer Vision and Pattern Recognition (CVPR), IEEE, New Orleans, LA, USA. pp. 7916–7925. doi:10.1109/CVPR52688.2022.00777.
- Rosell Polo, J.R., Sanz, R., Llorens, J., Arnó, J., Escolà, A., Ribes-Dasi, M., Masip, J., Camp, F., Gràcia, F., Solanelles, F., Pallejà, T., Val, L., Planas, S., Gil, E., Palacín, J., 2009. A tractor-mounted scanning LIDAR for the non-destructive measurement of vegetative volume and surface area of tree-row plantations: A comparison with conventional destructive measurements. *Biosystems Engineering* 102, 128–134. doi:10.1016/j.biosystemseng.2008.10.009.
- Seitz, S., Curless, B., Diebel, J., Scharstein, D., Szeliski, R., 2006. A Comparison and Evaluation of Multi-View Stereo Reconstruction Algorithms, in: 2006 IEEE Computer Society Conference on Computer Vision and Pattern Recognition (CVPR’06), pp. 519–528. doi:10.1109/CVPR.2006.19.
- Slafer, G., Elía, M., Savin, R., García, G., Terrile, I., Ferrante, A., Miralles, D., González, F., 2015. Fruiting efficiency: An alternative trait to further rise wheat yield. *Food and Energy Security* 4. doi:10.1002/fes3.59.
- Soltani, M., Omid, M., Alimardani, R., 2015. Egg volume prediction using machine vision technique based on pappus theorem and artificial neural network. *Journal of Food Science and Technology* 52, 3065–3071. doi:10.1007/s13197-014-1350-6.

- Steinbrener, J., Dimitrievska, V., Pittino, F., Starmans, F., Waldner, R., Holzbauer, J., Arnold, T., 2023. Learning metric volume estimation of fruits and vegetables from short monocular video sequences. *Heliyon* 9, e14722. doi:10.1016/j.heliyon.2023.e14722.
- Strange, H., Zwiggelaar, R., Sturrock, C., Mooney, S.J., Doonan, J.H., 2015. Automatic estimation of wheat grain morphometry from computed tomography data. *Functional plant biology: FPB* 42, 452–459. doi:10.1071/FP14068.
- Su, Q., Kondo, N., Li, M., Sun, H., Al Riza, D.F., 2017. Potato feature prediction based on machine vision and 3D model rebuilding. *Computers and Electronics in Agriculture* 137, 41–51. doi:10.1016/j.compag.2017.03.020.
- Uluişik, S., Yildiz, F., Özdemir, A.T., 2018. Image processing based machine vision system for tomato volume estimation, in: 2018 Electric Electronics, Computer Science, Biomedical Engineerings' Meeting (EBBT), pp. 1–4. doi:10.1109/EBBT.2018.8391460.
- Vivek Venkatesh, G., S. Md., I., A., G., and Ganesan, D., 2015. Estimation of Volume and Mass of Axi-Symmetric Fruits Using Image Processing Technique. *International Journal of Food Properties* 18, 608–626. doi:10.1080/10942912.2013.831444.
- Walker, C., Panozzo, J., 2011. Development of a small scale method to determine volume and density of individual barley kernels, and the relationship between grain density and endosperm hardness. *Journal of Cereal Science - J CEREAL SCI* 54. doi:10.1016/j.jcs.2011.06.008.
- Walker, C.K., Panozzo, J.F., 2012. Measuring volume and density of a barley grain using ellipsoid approximation from a 2-D digital image. *Journal of Cereal Science* 55, 61–68. doi:10.1016/j.jcs.2011.10.004.
- Wang, F., Li, F., Mohan, V., Dudley, R., Gu, D., Bryant, R., 2022. An unsupervised automatic measurement of wheat spike dimensions in dense 3D point clouds for field application. *Biosystems Engineering* 223, 103–114. doi:10.1016/j.biosystemseng.2021.11.022.
- Wang, Z., Zenkl, R., Greche, L., De Solan, B., Bernigaud Samatan, L., Ouahid, S., Visioni, A., Robles-Zazueta, C.A., Pinto, F., Perez-Olivera, I., Reynolds, M.P., Zhu, C., Liu, S., D'argaignon, M.P., Lopez-Lozano, R., Weiss, M., Marzougui, A., Roth, L., Dandrifosse, S., Carlier, A., Dumont, B., Mercatoris, B., Fernandez, J., Chapman, S., Najafian, K., Stavness, I., Wang, H., Guo, W., Virlet, N., Hawkesford, M.J., Chen, Z., David, E., Gillet, J., Irfan, K., Comar, A., Hund, A., 2025. The Global Wheat Full Semantic Organ Segmentation (GWSS) Dataset. doi:10.1101/2025.03.18.642594.
- Wasayangkool, K., Srisomboon, K., Lee, W., 2022. The Volume Estimation Technique using RSSI with Machine Learning in Manufacturing Process, in: 2022 37th International Technical Conference on Circuits/Systems, Computers and Communications (ITC-CSCC), pp. 1–4. doi:10.1109/ITC-CSCC55581.2022.9894869.
- van der Weth, C., 2019. ML-Toolkit: RNN Text Classifier in PyTorch. <https://github.com/chrisvdweth/ml-toolkit/blob/master/pytorch/models/text/classifier/rnn.py>. Accessed on June 19, 2025.
- Xiong, B., Wang, B., Xiong, S., Lin, C., Yuan, X., 2019. 3D Morphological Processing for Wheat Spike Phenotypes Using Computed Tomography Images. *Remote Sensing* 11, 1110. doi:10.3390/rs11091110.
- Xu, C., He, Y., Khannan, N., Parra, A., Boushey, C., Delp, E., 2013. Image-based food volume estimation, in: Proceedings of the 5th International Workshop on Multimedia for Cooking & Eating Activities, Association for Computing Machinery, New York, NY, USA. pp. 75–80. doi:10.1145/2506023.2506037.
- Yu, J., Lin, Z., Yang, J., Shen, X., Lu, X., Huang, T., 2019. Free-Form Image Inpainting with Gated Convolution. doi:10.48550/arXiv.1806.03589, arXiv:1806.03589.
- Zhang, D., Gajardo, J., Medic, T., Katircioglu, I., Boss, M., Kirchgessner, N., Walter, A., Roth, L., 2025. Wheat3dgs: In-field 3d reconstruction, instance segmentation and phenotyping of wheat heads with gaussian splatting, in: Proceedings of the Computer Vision and Pattern Recognition Conference (CVPR) Workshops, pp. 5360–5370.
- Zhang, T.Y., Suen, C.Y., 1984. A fast parallel algorithm for thinning digital patterns. *Communications of the ACM* 27, 236–239. doi:10.1145/357994.358023.
- Zhou, H., Riche, A.B., Hawkesford, M.J., Whalley, W.R., Atkinson, B.S., Sturrock, C.J., Mooney, S.J., 2021. Determination of wheat spike and spikelet architecture and grain traits using X-ray Computed Tomography imaging. *Plant Methods* 17, 26. doi:10.1186/s13007-021-00726-5.
- Zhou, Q.Y., Park, J., Koltun, V., 2018. Open3D: A Modern Library for 3D Data Processing. doi:10.48550/arXiv.1801.09847, arXiv:1801.09847.